Icarus 200 (2009) 292–303

Contents lists available at ScienceDirect

Icarus

www.elsevier.com/locate/icarus

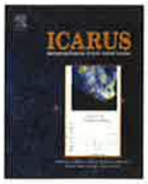

The correlated colors of transneptunian binaries

S.D. Benecchi [a,*,1], K.S. Noll [a], W.M. Grundy [b], M.W. Buie [b,c], D.C. Stephens [d], H.F. Levison [c]

[a] *Space Telescope Science Institute, 3700 San Martin Dr., Baltimore, MD 21218, USA*
[b] *Lowell Observatory, 1400 W. Mars Hill Rd., Flagstaff, AZ 86001, USA*
[c] *Department of Space Studies, Southwest Research Institute, 1050 Walnut Street 400, Boulder, CO 80302, USA*
[d] *Brigham Young University, Department of Physics and Astronomy, N145 ESC, Provo, UT 84602, USA*

ARTICLE INFO

Article history:
Received 29 July 2008
Revised 21 October 2008
Accepted 31 October 2008
Available online 27 November 2008

Keywords:
Hubble space telescope observations
Satellites, composition
Kuiper belt
Satellites of asteroids
Photometry

ABSTRACT

We report resolved photometry of the primary and secondary components of 23 transneptunian binaries obtained with the Hubble Space Telescope. V–I colors of the components range from 0.7 to 1.5 with a median uncertainty of 0.06 magnitudes. The colors of the primaries and secondaries are correlated with a Spearman rank correlation probability of 99.99991%, 5 sigma for a normal distribution. Fits to the primary vs. secondary colors are identical to within measurement uncertainties. The color range of binaries as a group is indistinguishable from that of the larger population of apparently single transneptunian objects. Whatever mechanism produced the colors of apparently single TNOs acted equally on binary systems. The most likely explanation is that the colors of transneptunian objects and binaries alike are primordial and indicative of their origin in a locally homogeneous, globally heterogeneous protoplanetary disk.

Published by Elsevier Inc.

1. Introduction

Transneptunian objects (TNOs) have long been known to display a surprisingly diverse range of colors (Jewitt and Luu, 1998). In some cases these colors have been correlated with dynamical properties (e.g. Tegler and Romanishin, 2000; Trujillo and Brown, 2002; Peixhino et al., 2004; Gulbis et al., 2006; Doressoundiram et al., 2008), although usually at low statistical significance. It has remained uncertain whether the large range of TNO colors is caused by differences in primordial chemical composition or by environmental factors such as the interplay of impact resurfacing and space weathering (Luu and Jewitt, 1996; Thébault and Doressoundiram, 2003). Color measurements have been made at both visible and infrared wavelengths (Gil-Hutton and Licandro, 2001; Jewitt and Luu, 2001; Delsanti et al., 2001, 2004; Doressoundiram et al., 2002, 2005; Stephens et al., 2003; McBride et al., 2003; Bauer et al., 2003; Peixinho et al., 2004). The largest compilations of these colors are contained in the MBOSS (Minor Bodies in the Outer Solar System; Hainaut and Delsanti, 2002) and HST (Stephens and Noll, 2007) databases. At optical wavelengths (B through J bands), most TNOs have been found to be spectrophotometrically featureless, but they differ from one another in slope (Boehnhardt et al., 2002; Peixinho et al., 2004). Attempts to model the spectrum shortward of 1000 nm have generally assumed a variable mixture of red organic material and a spectrally gray material (Brunetto and Roush, 2008; Grundy, 2009).

Unresolved colors have been obtained for about half of the more than 50 known transneptunian binaries (TNBs), but colors of resolved binary components have been reported for only 8 TNBs (Noll et al., 2008a). For many of the resolved measurements, the uncertainties are large (Noll et al., 2002, 2004a, 2004b; Osip et al., 2003) or unstated (Margot et al., 2005). No clear trends are identifiable from this small sample, although in most cases the colors of the components are similar.

In this work we present color photometry of the primary and secondary components of 23 TNBs using images from the Hubble Space Telescope (HST). We report photometry derived from both newly acquired observations and reanalyzed archival data. By using an improved point-spread-function-fitting technique we can achieve smaller uncertainties than previous work. With this new, uniformly reduced data we are able, for the first time, to definitively address the question of the colors of TNBs. As we show, these colors have implications for TNOs as a whole and their origins in the protoplanetary disk.

2. Observations

In this work we report color photometry from the Wide Field Planetary Camera 2 (WFPC2) and the Advanced Camera for Surveys High Resolution Camera (HRC) from seven HST programs. The colors of 13 TNBs reported here were measured as part of program 11178 (Grundy et al., 2009). It used the WFPC2 camera to measure TNB colors during a single epoch (normally spanning two

---

[*] Corresponding author. Fax: +1 410 338 5090.
E-mail address: susank@stsci.edu (S.D. Benecchi).
[1] Née S.D. Kern.

0019-1035/$ – see front matter Published by Elsevier Inc.
doi:10.1016/j.icarus.2008.10.025

96-min HST orbits, occasionally spanning three) using the 'wide V' F606W filter and the 'wide I' F814W filter. The filters are centered at 600.1 and 799.6 nm with FWHM of 150.2 and 152.2 nm, respectively (Heyer and Biretta, 2004). The observation sequence was two exposures in F606W (260 s each) followed by two exposures in F814W (500 s each) for the first orbit, and then the same sequence in reverse order for the second orbit. Bracketing the observations by F606W exposures helped to identify possible effects due to short-period lightcurve variability, which we discuss in Section 5.4. The four exposures in each filter were dithered using a sub-pixel dither pattern offset by (11.0, 5.5), (16.5, 16.5) and (5.5, 11.0) pixels relative to the first exposure.

We have measured the colors of 19 binaries in program 11178, but in 6 cases the color measurements were obtained when the components were separated by less than one PC pixel (45 milliarcsec). Because of the difficulty in resolving components at such small separations, we have excluded (80806) 2000 CM_{105}, (82075) 2000 YW_{183} (119979) 2002 WC_{19}, (182933) 2002 GZ_{31}, 2001 FL_{185} and 1999 RT_{214} from our analysis of resolved colors, but include them in the comparison of unresolved colors in Section 5.1.

HST programs 10508, 9991 and 9746 obtained color measurements of 8 TNBs using the HRC (Margot et al., 2005; Stansberry et al., 2006; Grundy et al., 2007, 2008). Three additional HST programs 9259, 9320 and 9508, obtained WFPC2 observations of a single TNB, 1998 WW_{31}, over multiple epochs (Veillet et al., 2002). A summary of each HST program analyzed in this study can be found in Table 1.

For completeness in our analysis we have included the resolved ground based colors of two additional TNBs, (88611) Teharonhiawako/Sawiskera and 2005 EO_{304}. These data were obtained at Las Campanas Observatory from the 6.5-m Clay telescope using the Raymond and Beverly Sackler Magellan Instant Camera (MagIC, Osip et al., 2004) under excellent (<0.5 arcsec) seeing conditions. Analysis of these images is detailed in Kern (2006).

3. Data reduction and analysis

3.1. Pipeline processing

We processed the data through the standard HST pipeline (Baggett et al., 2002; Pavlovsky, 2006). This software performs basic image reduction: it flags static bad pixels, performs A/D correction,[2] subtracts the bias, and dark images, and corrects for flat fielding. It also updates the header with the appropriate photometry keywords. The flat-field-calibrated images, subscripted by *c0f* for WFPC2 and *flt* for HRC, were the ones we analyzed.

3.2. Point-spread function fitting

In simplest terms, our analysis process fits a model point-spread function (PSF) generated by the Tiny Tim program (Krist and Hook, 2004, v6.3) to the data to determine the locations of the binary components and to perform photometry. The detailed steps differ slightly between instruments with additional steps being required on ACS images due to its larger geometric distortion. In the following text we describe the steps required for ACS. The WFPC2 analysis is very similar; it is described in full detail in Grundy et al. (2008).

3.2.1. Object identification and initial values

We began our PSF-fitting by estimating the center position of each binary component by eye (good to about 0.5 pixels) and by summing the object flux in a 1.5 pixel radius around that position. Calculations were carried out in a sub-image, 20–60 pixels on a side, centered on the primary component. We defined the sub-image to be large enough to encompass both components of the binary and to ensure sufficient sky so that the background can be computed. Bad pixels from cosmic rays and hot pixels within the sub-image were flagged and ignored in further calculations prior to determining the background.

3.2.2. Model images

We further refined our initial guesses for object positions and fluxes by creating a series of scaled and sub-sampled Tiny Tim PSFs generated for a solar spectral distribution [models 51 (HD 150205, a G5V star) and 57 (HD 154712, a K4V star) from the Bruzual–Persson–Gunn–Stryker Spectra Library; Krist and Hook, 2004] around the estimated positions of each component. A new sub-sampled PSF was created for each whole pixel location and sub-pixel shifting was performed before re-sampling the model to match the image pixel scale. Additionally, the PSF was modified to account for changes in the focus due to small thermally-induced changes known as "breathing" and for small motions of the spacecraft known as "jitter" that occur on orbital timescales. The first effect is modeled by the z4 parameter in the input file for Tiny Tim. The second effect is modeled by convolving the model with a smearing Gaussian. The determination of these two effects is iterative after the initial values for the binary components are refined. The focus and smearing values that yield a minimization of the χ^2 residual was defined to be the best focus and smearing value for the image. We found for the HRC data that focus was an important parameter to determine. For the WFPC2 data, the default focus value was adequate in most cases and no further adjustments were justified.

3.2.3. Refined PSF fit

We determined each of seven components, average background, position $(x1, y1)$ and flux $(f1)$ of the primary and position $(x2, y2)$ and flux $(f2)$ of the secondary individually by minimizing the χ^2 of the residual between the model and the sub-image. Once all the position (x, y) and flux scaling (f) were refined we re-determined the average background. This process resulted in a refined initial guess that was sufficient to enable automated fitting to proceed in most cases. The automated fitting employed the *amoeba* (Press et al., 1992) routine, which performs multidimensional minimization of a function containing all our variables using the downhill simplex method, to optimize the fits. We ran the automated process alternating with the focusing routine until the χ^2 converged. Typically, 4–5 iterations were required to reach a final PSF model.

3.2.4. Photometry

Before extracting photometry from the model images it was necessary to make an additional correction for the geometric distortion in the HRC data. The flat-field-corrected (*flt*) images were background subtracted and multiplied by a "pixel area map" (PAM) correction image prior to the PSF fitting. At the location on the HRC where our data fell the PAM correction is a factor of ~1.12. The PAM correction does not affect the fitted position and no similar correction was necessary for WFPC2 images.

We extracted photometry from the final PSF model for each component of the binary. Counts were summed within a 0.5 arcsec aperture and converted to magnitude in the standard fashion, $M_{\text{half}} = -2.5\log_{10}(\text{counts/s})$. This value was then corrected to an infinite aperture by adding an offset value, ΔM_{inf}, from Table 5 in Sirianni et al. (2005). The photometric zero point, M_{Zpt}, was determined from the *photflam* and *photzpt* values in the image header. It is given in the standard Space Telescope

---

[2] A/D correction takes the observed charge in each pixel in the CCD and converts it to a digital number with the appropriate gain setting. The gain for WFPC2 is 7.12 and for ACS is 2.216.

Table 1
Log of observations.

PropID	PI	No. obj	Camera	Filters/observing sequence
11178	W.M. Grundy	12	WFPC2	2 × F606W (260 s), 4 × F814W (500 s), 2 × F606W (260 s) dithered
10508	W.M. Grundy	3	ACS/HRC	2 × F606W (223 s), 4 × F814W (223 s), 2 × F606W (223 s) dithered
9991	K.S. Noll	1	ACS/HRC	2 × F775W (500 s), 2 × F475W (600 s)
9746	J.L. Margot	4	ACS/HRC	2 × F606W (610 s), 2 × F814W (610 s)
9508	C. Veillet	1	WFPC2	Various combinations of F555W (500, 600 s), F675W (500, 700 s) and F814W (500, 600 s)
9259	C. Veillet	1	WFPC2	2 × F555W (230 s), 2 × F675W (230 s), 2 × F814W (300 s)
9320	C. Veillet	1	WFPC2	2 × F555W (230 s), 2 × F675W (230 s), 2 × F814W (300 s)

magnitude system (STmag). We used *synphot* to convert from the STmag system to the standard Vega magnitude system (Vegamag, M_{Vega}). The conversions are $M_{\text{Vega}}(\text{F606W, WFPC2}) = -0.2989$, $M_{\text{Vega}}(\text{F814W, WFPC2}) = -1.2376$, $M_{\text{Vega}}(\text{F606W, HRC}) = -0.2369$, and $M_{\text{Vega}}(\text{F814W, WFPC2}) = -1.28$.

A correction for the location- and flux-dependent charge transfer efficiency (CTE) is also required for HST data. For the HRC we followed the process described in Riess (2003) and for WFPC2 the example of Dolphin (2000a, 2000b). The correction for CTE losses is on the order of -0.05 magnitudes for both instruments.

Uncertainties were estimated in two ways. For individual *flt* or *c0f* images we determined the changes in flux that caused a 1-sigma change in the χ^2 residual. Additionally, for groups of exposures taken in a single 2–3 orbit visit we computed the standard deviation using the corrected two-pass algorithm (Press et al., 1992). We found that the standard deviation from multiple exposures was comparable to or a few hundredths magnitude larger than the uncertainty calculated from the individual exposures. In all cases we report the largest uncertainty obtained from these two methods. We note that short period lightcurves are one potential source of systematic "noise" in our photometry that might increase the standard deviation as discussed in Section 5.4.

3.2.5. *Color correction*

In order to compare the HST measurements with other color values in the literature we converted from the native HST filter photometry to Johnson V and Cousins I magnitudes using *synphot*. The color corrections, ΔM_{STD} used a reddened Kurucz model solar spectrum convolved with the appropriate filter profiles. The reddening, E(B–V), was computed from the F606W–F814W color and ranged from 0.15 to 0.6. The color corrections were 0.20–0.40 magnitudes for F606W to Johnson V (V is fainter than F606W) and 0.01–0.05 magnitudes for F814W to Cousins I (I is fainter than F814W).

3.2.6. *Photometry summary*

Our final calibrated magnitude, M_c in the measured filter (i.e. in the F606W filter $M_c = M_{\text{F606W}}$, in the F814W $M_c = M_{\text{F814W}}$) for each object listed in Table 2 is based on the terms found in

$$M_c = M_{\text{half}} + \Delta M_{\text{inf}} + M_{\text{Zpt}} + \text{CTE} + M_{\text{vega}}. \tag{1}$$

Objects are sorted by the color of the primary component (within each native filter sample pair) and the second to last column tabulates the difference between the primary and secondary components. In most cases this difference is small, <0.1 magnitudes. The standard filter colors V and I, tabulated in Table 3 and again sorted relative to the color of the primary component, were calculated with the addition of the color correction factor, F_{STD}, appropriate for conversion from the respective native filters. In Appendix A we document a complete example of our photometry pipeline. We include the V–I colors for the combined light of the 6 unresolved binary systems in Table 3 since we find in Section 4 that the colors of the individual components are nearly identical.

Table 3 includes calculation of the spectral gradient, S, of our observations for more direct comparison with surveys in various filters. The spectral gradient is calculated following Boehnhardt et al. (2001). It is a measure of the reddening of the reflectance spectrum between two wavelengths, $\lambda = 547.9$ nm (Johnson V) and some other wavelength [in the case of this paper either $\lambda = 689.8$ nm (Johnson R) or $\lambda = 787.4$ nm (Cousins I)], expressed in percent of reddening per 100 nm. A value of $S = 0.0$ means the object has exactly solar colors.

4. Statistical analysis

A plot of the color of the primary vs. the color of the secondary of each binary system is found in Fig. 1. As can be seen by inspection, the colors of the components are clearly correlated. We quantified the correlation using two different statistical measures, the Spearman rank correlation and the Pearson product-moment coefficient. We describe each briefly.

The Spearman rank correlation is a non-parametric statistical test that does not make any assumptions about the functional form of a possible correlation and does not assume a normal distribution of either variable. The independent variable, in this case the color of the primary, is ranked in order of increasing F606W–F814W color. The secondaries are similarly ranked and the correlation coefficient measures the difference between these two rankings. In a noiseless, perfectly correlated data set the rankings would be identical. Using the data in Table 2, we find a Spearman rank coefficient of $\rho = 0.8008$, corresponding to 99.99991% probability (5 sigma for a normal distribution) that the colors are correlated.

As a second check we computed the Pearson product-moment coefficient for the measured F606W–F814W colors. The Pearson product-moment coefficient applies to situations where the possible relationship between variables is linear. Other than linearity, there are no assumptions about the distribution, in particular it need not be normal. We find a Pearson product moment coefficient of $r = 0.84$. Using a probability table we find that the primary and secondary colors are correlated at a significance much more than 99%, in agreement with the Spearman rank test.

Two variables can be correlated, but systematically offset from one another. In order to determine whether there are any color offsets between primaries and secondaries in our sample we performed an additional test. In Fig. 1 the dashed line is the locus of identical component colors which, by definition, goes through the origin. The best-fit line with a slope of 1 has a y-intercept of 0.01 ± 0.01 magnitudes. Thus, to the limit of our measurement uncertainties, the colors of primaries and secondaries are consistent with identical colors. We conclude that binary colors are not only correlated, but are statistically identical.

5. Discussion

5.1. *Comparison to ground based photometry*

In Table 4 we list derived absolute magnitudes for the combined (primary + secondary) light of TNBs at zero phase angle, $H_V(1,1,0)$ or simply H_V. We also tabulate the spectral gradient,

Table 2
Resolved HST magnitudes.

Object	MJD[a]	Separation (arcsec)	Δ*M* F606W	Primary			Secondary			ΔColor[b]	Ref.
				F606W	F814W	Color[b]	F606W	F814W	Color[b]		
2000 QL$_{251}$	54339.75743	0.267 ± 0.001	0.27 ± 0.09	23.36 ± 0.07	22.76 ± 0.03	0.60 ± 0.07	23.63 ± 0.06	22.90 ± 0.09	0.73 ± 0.10	−0.13 ± 0.13	1
(120347) 2004 SB$_{60}$	54324.32378	0.156 ± 0.002	2.19 ± 0.02	20.66 ± 0.01	20.04 ± 0.01	0.62 ± 0.01	22.85 ± 0.02	22.22 ± 0.04	0.63 ± 0.04	−0.01 ± 0.04	1
2001 QC$_{298}$	53175.67839	0.108 ± 0.001	0.51 ± 0.04	23.07 ± 0.02	22.45 ± 0.03	0.62 ± 0.04	23.58 ± 0.03	22.90 ± 0.03	0.68 ± 0.04	−0.07 ± 0.06	3
(60458) 2000 CM$_{114}$[c]	54483.41189	0.082 ± 0.002	0.60 ± 0.08	23.90 ± 0.04	23.29 ± 0.08	0.62 ± 0.09	24.50 ± 0.07	23.75 ± 0.08	0.75 ± 0.11	−0.13 ± 0.14	1
2001 XR$_{254}$	54439.41264	0.105 ± 0.001	0.07 ± 0.09	23.06 ± 0.05	22.32 ± 0.07	0.74 ± 0.09	23.12 ± 0.07	22.36 ± 0.07	0.76 ± 0.10	−0.02 ± 0.13	1
(42355) Typhon	53780.55666	0.169 ± 0.001	1.32 ± 0.03	20.05 ± 0.03	19.23 ± 0.01	0.83 ± 0.03	21.38 ± 0.02	20.61 ± 0.02	0.77 ± 0.02	0.06 ± 0.04	2
	53785.07234	0.160 ± 0.001	1.36 ± 0.04	20.11 ± 0.02	19.35 ± 0.05	0.77 ± 0.06	21.47 ± 0.03	20.78 ± 0.02	0.70 ± 0.04	0.07 ± 0.07	2
	54044.06850	0.135 ± 0.001	1.05 ± 0.03	20.62 ± 0.03	19.91 ± 0.01	0.72 ± 0.03	21.68 ± 0.02	20.98 ± 0.01	0.69 ± 0.02	0.02 ± 0.03	2
	54091.45205	0.102 ± 0.001	1.23 ± 0.04	20.55 ± 0.02	19.77 ± 0.01	0.78 ± 0.02	21.78 ± 0.03	21.01 ± 0.02	0.77 ± 0.04	0.01 ± 0.04	2
(134860) 2000 OJ$_{67}$	54319.38434	0.073 ± 0.001	0.82 ± 0.05	22.88 ± 0.03	22.08 ± 0.05	0.80 ± 0.06	23.70 ± 0.04	22.66 ± 0.03	1.04 ± 0.05	−0.24 ± 0.07	1
2004 PB$_{108}$	54375.28295	0.300 ± 0.003	1.11 ± 0.09	23.56 ± 0.04	22.76 ± 0.05	0.80 ± 0.06	24.67 ± 0.08	23.83 ± 0.09	0.84 ± 0.12	−0.04 ± 0.13	1
(58534) Logos	53179.04682	0.072 ± 0.001	0.33 ± 0.06	23.48 ± 0.04	22.65 ± 0.05	0.83 ± 0.07	23.81 ± 0.04	22.93 ± 0.17	0.88 ± 0.17	−0.04 ± 0.18	3
(65489) Ceto	53861.31526	0.084 ± 0.002	0.57 ± 0.03	21.23 ± 0.02	20.30 ± 0.09	0.94 ± 0.09	21.80 ± 0.03	20.97 ± 0.02	0.83 ± 0.03	0.11 ± 0.10	2
	53865.18174	0.087 ± 0.001	0.60 ± 0.03	21.14 ± 0.03	20.35 ± 0.02	0.79 ± 0.03	21.75 ± 0.01	20.92 ± 0.03	0.82 ± 0.03	−0.03 ± 0.04	2
	53885.00662	0.083 ± 0.001	0.54 ± 0.09	21.31 ± 0.02	20.44 ± 0.01	0.87 ± 0.02	21.85 ± 0.08	21.09 ± 0.02	0.76 ± 0.09	0.11 ± 0.09	2
	53886.07239	0.087 ± 0.001	0.60 ± 0.02	21.28 ± 0.01	20.47 ± 0.01	0.82 ± 0.02	21.88 ± 0.02	21.10 ± 0.02	0.78 ± 0.03	0.04 ± 0.03	2
2003 TJ$_{58}$	54324.06038	0.090 ± 0.002	0.44 ± 0.09	24.02 ± 0.05	23.06 ± 0.06	0.96 ± 0.08	24.46 ± 0.08	23.74 ± 0.07	0.72 ± 0.10	0.24 ± 0.13	1
	54346.09499	0.133 ± 0.001	0.51 ± 0.09	24.01 ± 0.06	23.15 ± 0.04	0.86 ± 0.07	24.51 ± 0.08	23.60 ± 0.06	0.92 ± 0.10	−0.06 ± 0.12	1
	54395.70344	0.171 ± 0.001	0.52 ± 0.10	23.88 ± 0.05	23.01 ± 0.04	0.87 ± 0.07	24.41 ± 0.08	23.50 ± 0.06	0.90 ± 0.10	−0.03 ± 0.12	1
	54424.24945	0.134 ± 0.001	0.55 ± 0.08	23.81 ± 0.04	22.90 ± 0.03	0.90 ± 0.05	24.36 ± 0.07	23.43 ± 0.06	0.93 ± 0.09	−0.03 ± 0.10	1
2003 QW$_{111}$	54682.80058	0.169 ± 0.002	1.38 ± 0.17	23.55 ± 0.04	22.69 ± 0.03	0.86 ± 0.05	24.92 ± 0.14	23.96 ± 0.09	0.97 ± 0.16	−0.11 ± 0.16	1
	54698.64919	0.284 ± 0.001	1.42 ± 0.15	23.57 ± 0.04	22.60 ± 0.04	0.97 ± 0.07	24.99 ± 0.15	24.09 ± 0.09	0.90 ± 0.17	0.07 ± 0.17	1
1999 OJ$_{4}$	54336.36316	0.107 ± 0.001	0.15 ± 0.22	23.56 ± 0.06	22.67 ± 0.07	0.89 ± 0.09	23.70 ± 0.21	22.69 ± 0.03	1.01 ± 0.21	−0.12 ± 0.23	1
(79360) 1997 CS$_{29}$	54457.58469	0.089 ± 0.001	0.19 ± 0.03	22.37 ± 0.03	21.47 ± 0.01	0.90 ± 0.03	22.57 ± 0.02	21.60 ± 0.04	0.96 ± 0.04	−0.07 ± 0.05	1
(123509) 2000 WK$_{183}$[c]	54389.84163	0.068 ± 0.003	0.05 ± 0.05	23.58 ± 0.03	22.66 ± 0.02	0.92 ± 0.04	23.62 ± 0.03	22.76 ± 0.03	0.86 ± 0.05	0.06 ± 0.06	1
(148780) 2001 UQ$_{18}$	54416.37948	0.157 ± 0.001	0.45 ± 0.13	23.19 ± 0.10	22.27 ± 0.08	0.92 ± 0.13	23.64 ± 0.08	22.63 ± 0.11	1.01 ± 0.14	−0.09 ± 0.18	1
(47171) 1999 TC$_{36}$	53594.96925	0.282 ± 0.001	2.21 ± 0.02	20.06 ± 0.01	19.11 ± 0.01	0.95 ± 0.01	22.27 ± 0.01	21.40 ± 0.02	0.88 ± 0.02	0.07 ± 0.03	3
2000 CF$_{105}$	53155.17593	0.626 ± 0.001	0.70 ± 0.16	24.02 ± 0.11	23.05 ± 0.05	0.97 ± 0.12	24.72 ± 0.12	23.81 ± 0.05	0.92 ± 0.13	0.05 ± 0.18	3
2000 CQ$_{114}$	54548.37046	0.196 ± 0.001	0.12 ± 0.19	24.16 ± 0.04	23.16 ± 0.05	0.99 ± 0.06	24.27 ± 0.18	23.32 ± 0.06	1.04 ± 0.15	0.05 ± 0.22	1
2001 QY$_{297}$	54586.87578	0.173 ± 0.016	0.21 ± 0.27	22.91 ± 0.15	21.85 ± 0.10	1.05 ± 0.18	23.11 ± 0.22	22.30 ± 0.14	0.82 ± 0.26	0.23 ± 0.32	1
2003 QY$_{90}$	53576.09906	0.363 ± 0.002	0.02 ± 0.13	23.87 ± 0.04	22.78 ± 0.16	1.10 ± 0.16	23.89 ± 0.12	22.85 ± 0.09	1.04 ± 0.15	0.05 ± 0.22	2
	53596.96684	0.358 ± 0.001	−0.11 ± 0.06	23.88 ± 0.05	22.82 ± 0.05	1.06 ± 0.07	23.77 ± 0.03	22.69 ± 0.05	1.08 ± 0.06	−0.01 ± 0.09	2
	53617.48881	0.337 ± 0.002	0.41 ± 0.11	23.87 ± 0.02	22.84 ± 0.04	1.04 ± 0.04	24.28 ± 0.11	23.14 ± 0.09	1.14 ± 0.14	−0.11 ± 0.15	2
	53995.87532	0.195 ± 0.003	0.17 ± 0.12	23.86 ± 0.02	22.76 ± 0.05	1.09 ± 0.05	24.03 ± 0.12	23.07 ± 0.04	0.95 ± 0.12	0.14 ± 0.13	2
(26308) 1998 SM$_{165}$	53921.93540	0.295 ± 0.001	2.20 ± 0.05	21.63 ± 0.02	20.51 ± 0.02	1.12 ± 0.03	23.83 ± 0.04	22.79 ± 0.01	1.04 ± 0.04	0.08 ± 0.05	3
Object	MJD[a]	Separation (arcsec)	Δ*M* F555W	Primary			Secondary			ΔColor[b]	Ref.
				F555W	F814W	Color[b]	F555W	F814W	Color[b]		
1998 WW$_{31}$	52102.88866	0.881 ± 0.002	0.49 ± 0.19	24.04 ± 0.13	22.91 ± 0.06	1.13 ± 0.14	24.53 ± 0.14	23.59 ± 0.08	0.94 ± 0.16	0.19 ± 0.21	5
	52130.78102	0.783 ± 0.008	0.17 ± 0.02	24.17 ± 0.01	23.33 ± 0.24	0.84 ± 0.24	24.34 ± 0.01	23.04 ± 0.38	1.31 ± 0.38	−0.47 ± 0.45	5
	52162.67546	0.589 ± 0.002	−0.07 ± 0.05	24.45 ± 0.03	23.09 ± 0.09	1.37 ± 0.09	24.38 ± 0.04	23.61 ± 0.16	0.77 ± 0.16	0.60 ± 0.19	5
	52273.47616	0.416 ± 0.002	0.64 ± 0.05	23.82 ± 0.03	22.97 ± 0.03	0.84 ± 0.04	24.45 ± 0.05	23.34 ± 0.15	1.11 ± 0.16	−0.27 ± 0.16	6
	52293.51297	0.562 ± 0.002	0.40 ± 0.02	24.03 ± 0.01	23.04 ± 0.03	0.99 ± 0.03	24.42 ± 0.02	23.69 ± 0.03	0.74 ± 0.04	0.25 ± 0.05	6
	52329.22130	0.767 ± 0.003	0.76 ± 0.24	24.03 ± 0.08	22.93 ± 0.17	1.10 ± 0.18	24.78 ± 0.23	23.61 ± 0.04	1.17 ± 0.23	−0.08 ± 0.30	6
Object	MJD[a]	Separation (arcsec)	Δ*M* F475W	Primary			Secondary			ΔColor[b]	Ref.
				F475W	F775W	Color[b]	F475W	F775W	Color[b]		
(66652) Borasisi	52871.61183	0.075 ± 0.001	0.55 ± 0.30	23.29 ± 0.09	21.50 ± 0.05	1.79 ± 0.10	23.84 ± 0.29	21.81 ± 0.03	2.03 ± 0.29	−0.24 ± 0.31	4
	52897.24733	0.228 ± 0.001	0.52 ± 0.08	23.34 ± 0.05	21.49 ± 0.03	1.85 ± 0.06	23.87 ± 0.07	21.88 ± 0.06	1.99 ± 0.09	−0.14 ± 0.11	4
	52960.50017	0.103 ± 0.001	0.47 ± 0.09	23.44 ± 0.03	21.68 ± 0.01	1.76 ± 0.04	23.91 ± 0.08	22.06 ± 0.02	1.85 ± 0.08	−0.09 ± 0.09	4
	52972.30088	0.079 ± 0.001	0.45 ± 0.04	23.38 ± 0.02	21.65 ± 0.05	1.72 ± 0.05	23.82 ± 0.03	22.05 ± 0.01	1.77 ± 0.03	−0.05 ± 0.06	4

(*continued on next page*)

Table 2 (*continued*)

Object	MJD[a]	Separation (arcsec)	ΔM Sloan r	Primary			Secondary			ΔColor[b]	Ref.
				Sloan r'	Sloan i'	Color[b]	Sloan r'	Sloan r'	Color[b]		
(88611) Teharon[d]	53261.13940	0.712 ± 0.005	0.56 ± 0.02	22.79 ± 0.01	22.34 ± 0.02	0.45 ± 0.02	23.35 ± 0.02	22.91 ± 0.03	0.44 ± 0.03	0.01 ± 0.03	7
2005 EO_{304}	53849.68608	2.069 ± 0.009	1.53 ± 0.12	22.69 ± 0.08	21.81 ± 0.10	0.88 ± 0.10	24.22 ± 0.12	23.40 ± 0.13	0.82 ± 0.13	0.06 ± 0.13	7

(1) Program 11178, WFPC2; (2) Program 10508, ACS/HRC; (3) Program 9746, ACS/HRC; (4) Program 9991, ACS/HRC; (5) Program 9259, WFPC2; (6) Program 9230, WFPC2; (7) Ground based observations from Magellan with MagIC.

[a] MJD = JD-2400000.5, not light time corrected.

[b] Color is defined with respect to the two filters listed, i.e. F606W–F814W, F555W–F184W, F475W–F775W, and Sloan r'–Sloan i'.

[c] Secondary/primary ambiguous.

[d] Shorthand for Teharonhiawako.

S (Boehnhardt et al., 2001), for these measurements. We compare both H_V and S with published (or derived) values from other research teams. We include in this table the combined primary and secondary magnitudes for the four objects (listed in Section 2) that we did not resolve. We calculate H_V following the methodology described by Bowell et al. (1989) and discussed with specific application to TNOs by Romanishin and Tegler (2005). Following these authors, we used $G = 0.15$ for all the objects in the table. The details of the phase correction can be found at the end of Appendix A. We calculate S as described in Section 3.2.6. We use V–I and V–R color information from the sources referenced in the last column of Table 4.

Absolute magnitudes are published for all TNOs by the Minor Planet Center (MPC). We find, as have others (Romanishin and Tegler, 2005), that MPC magnitudes are in poor agreement with our photometry. In most cases we find that our values for H_V are fainter than the MPC's with a median difference of 0.3 magnitudes. We suggest, similar to Romanishin and Tegler (2005), that disagreements with the MPC database are the result of H_V magnitudes determined in the MPC from observations submitted from a variety of sites, transformed from a variety of filters and also based on measurements obtained for astrometric purposes instead of photometric accuracy.

Only 40% of our targets have reported photometric measurements in the literature. For those objects we find agreement with at least one literature measurement within the error bars for ~60% of our targets. However, we do find striking disagreement with some published values for a few of our targets; we comment on them briefly.

The largest disagreement we find is for (47171) 1999 TC_{36}. We found $H_V = 3.95 \pm 0.01$, more than 1 magnitude brighter than three other published values. (47171) 1999 TC_{36} is suspected to be a triple system (Jacobson and Margot, 2007) and has, in the past, been found to have an inconsistent lightcurve (Peixinho et al., 2002; Ortiz et al., 2003). However, we have no definitive explanation for this large discrepancy.

We also find a significant difference for (80806) 2000 CM_{105} where we measured $H_V = 7.10 \pm 0.09$, 0.8 magnitudes brighter than that found by Hainaut and Delsanti (2002). Lacerda and Luu (2006) put an upper limit on variability in this object of 0.14 magnitudes from relative photometry taken over a period of several hours on each of two different nights. There is, thus, little to suggest that the large difference we observe might be due to lightcurve variations.

In a few other cases magnitude differences may be the result of observations obtained at different points in the lightcurves of the objects. (65489) Ceto/Phorcys has been reported to have a lightcurve with an amplitude of 0.13 ± 0.02 magnitudes and a period of 4.43 ± 0.03 h (Barucci et al., 2008). (26308) 1998 SM_{165} is known to have an 8.40 ± 0.05 h period with an amplitude >0.45 magnitudes (Spencer et al., 2006). (82075) 2000 YW_{134}, and (79360) 1997 CS_{29} have been reported to have upper limits on variability of 0.10 magnitudes in observations taken sparsely over multiple nights (Sheppard and Jewitt, 2002, 2003). 1999 OJ_4 may have a lightcurve of a few tenths of a magnitude (Benecchi, unpublished data). Lastly, we note that (58534) Logos/Zoe gives a consistent H_V with other published measurements, but is known to exhibit large variability (Noll et al., 2002).

With respect to ground-based spectral slope we find that our S values for the combined pairs are consistent with the S values determined for datasets in the literature within the error bars with a few exceptions. (58534) Logos, and (47171) TC_{36} are both more neutral than literature values and (66652) Borasisi is more red. The later may be due, at least partially, to the color conversion offsets from F475W to V which are different than those used for the other objects we measured.

Table 3
Transformed Johnson/cousins magnitudes and colors.

Object	Primary				Secondary				Δ(V–I)	Type[c]
	H_V[a]	H_I[a]	(V–I)	S[b]	H_V[a]	H_I[a]	(V–I)	S[b]		
2001 QC$_{298}$	8.18 ± 0.03	7.40 ± 0.04	0.78 ± 0.05	1 ± 2	8.69 ± 0.04	7.84 ± 0.03	0.85 ± 0.05	1 ± 2	−0.07 ± 0.07	SD
Teharon	6.48 ± 0.02	5.66 ± 0.03	0.82 ± 0.04	1 ± 2	7.04 ± 0.03	6.23 ± 0.04	0.81 ± 0.05	1 ± 2	0.01 ± 0.06	CL
2000 QL$_{251}$	7.63 ± 0.08	6.78 ± 0.03	0.85 ± 0.09	2 ± 5	7.90 ± 0.07	6.92 ± 0.09	0.98 ± 0.12	7 ± 5	−0.13 ± 0.15	2:1
(120347)	4.39 ± 0.01	3.52 ± 0.01	0.87 ± 0.01	2 ± 1	6.58 ± 0.02	5.70 ± 0.04	0.89 ± 0.04	3 ± 2	−0.02 ± 0.04	SD
(60458)	7.91 ± 0.06	7.03 ± 0.08	0.87 ± 0.10	2 ± 5	8.50 ± 0.10	7.50 ± 0.08	1.00 ± 0.13	8 ± 6	−0.13 ± 0.16	SD
1998 WW$_{31}$	7.18 ± 0.01	6.21 ± 0.02	0.91 ± 0.02	6 ± 1	7.48 ± 0.01	6.78 ± 0.02	0.76 ± 0.03	1 ± 1	0.15 ± 0.04	CL
Typhon	8.02 ± 0.01	7.06 ± 0.01	0.96 ± 0.02	7 ± 1	9.21 ± 0.01	8.27 ± 0.01	0.93 ± 0.02	5 ± 1	0.03 ± 0.03	CN
2001 XR$_{254}$	6.82 ± 0.08	5.78 ± 0.07	1.04 ± 0.11	10 ± 5	6.89 ± 0.10	5.82 ± 0.07	1.06 ± 0.12	11 ± 6	−0.02 ± 0.16	CL
Ceto	6.94 ± 0.01	5.89 ± 0.01	1.05 ± 0.02	10 ± 1	7.50 ± 0.01	6.51 ± 0.01	1.01 ± 0.02	8 ± 1	0.04 ± 0.03	CN
Logos	7.31 ± 0.06	6.26 ± 0.06	1.05 ± 0.08	10 ± 4	7.64 ± 0.05	6.55 ± 0.17	1.09 ± 0.18	12 ± 8	−0.04 ± 0.20	CL
(134860)	6.87 ± 0.04	5.75 ± 0.05	1.12 ± 0.07	14 ± 3	7.69 ± 0.06	6.33 ± 0.03	1.36 ± 0.06	28 ± 3	−0.24 ± 0.09	CL
2004 PB$_{108}$	7.45 ± 0.05	6.33 ± 0.05	1.12 ± 0.07	14 ± 4	8.56 ± 0.10	7.40 ± 0.09	1.16 ± 0.13	16 ± 6	−0.04 ± 0.15	SD
2003 TJ$_{58}$	7.92 ± 0.03	6.79 ± 0.02	1.13 ± 0.04	14 ± 2	8.43 ± 0.04	7.32 ± 0.03	1.11 ± 0.05	13 ± 3	0.02 ± 0.06	CL
(47171)	4.08 ± 0.01	2.89 ± 0.01	1.19 ± 0.01	18 ± 1	6.30 ± 0.02	5.18 ± 0.02	1.12 ± 0.03	14 ± 1	0.07 ± 0.03	3:2
2001 FL$_{185}$	7.41 ± 0.21[d]	6.22 ± 0.10[d]	1.19 ± 0.23[d]	18 ± 12	–	–	–	–	–	CL
2000 CF$_{105}$	7.84 ± 0.14	6.63 ± 0.06	1.21 ± 0.15	19 ± 7	8.55 ± 0.15	7.38 ± 0.06	1.16 ± 0.16	16 ± 8	0.05 ± 0.22	CL
1999 OJ$_4$	8.15 ± 0.09	6.90 ± 0.08	1.25 ± 0.11	21 ± 6	8.29 ± 0.24	6.92 ± 0.03	1.37 ± 0.24	28 ± 11	−0.12 ± 0.26	CL
(82075)	4.85 ± 0.10[d]	3.60 ± 0.15[d]	1.25 ± 0.18[d]	21 ± 9	–	–	–	–	–	8:3
(79360)	6.27 ± 0.04	5.00 ± 0.01	1.26 ± 0.04	22 ± 2	6.46 ± 0.03	5.13 ± 0.04	1.33 ± 0.05	26 ± 2	−0.07 ± 0.06	CL
2003 QW$_{111}$	7.40 ± 0.05	8.81 ± 0.09	1.27 ± 0.04	23 ± 2	6.11 ± 0.02	7.50 ± 0.06	1.31 ± 0.12	25 ± 5	−0.04 ± 0.12	7:4
(119979)	4.88 ± 0.07[d]	3.60 ± 0.06[d]	1.28 ± 0.09[d]	23 ± 4	–	–	–	–	–	SD
(123509)	7.51 ± 0.05	6.22 ± 0.02	1.30 ± 0.05	24 ± 3	7.56 ± 0.04	6.32 ± 0.03	1.24 ± 0.06	20 ± 3	0.06 ± 0.08	CL
(148780)	6.98 ± 0.14	5.69 ± 0.08	1.30 ± 0.16	24 ± 8	7.43 ± 0.12	6.05 ± 0.11	1.39 ± 0.17	29 ± 8	−0.09 ± 0.24	CL
2003 QY$_{90}$	7.61 ± 0.02	6.29 ± 0.03	1.34 ± 0.04	25 ± 2	7.65 ± 0.04	6.41 ± 0.03	1.34 ± 0.06	22 ± 3	0.00 ± 0.07	CL
(80806)	7.10 ± 0.09[d]	5.75 ± 0.05[d]	1.34 ± 0.10[d]	26 ± 5	–	–	–	–	–	CL
(182933)	6.99 ± 0.06[d]	5.64 ± 0.02[d]	1.35 ± 0.06[d]	27 ± 2	–	–	–	–	–	SD
1999 RT$_{214}$	8.13 ± 0.02[d]	6.73 ± 0.06[d]	1.39 ± 0.06[d]	30 ± 2	–	–	–	–	–	CL
(26308)	6.11 ± 0.03	4.71 ± 0.02	1.40 ± 0.04	30 ± 2	8.31 ± 0.05	6.99 ± 0.01	1.32 ± 0.05	25 ± 2	0.08 ± 0.06	2:1
2000 CQ$_{114}$	7.92 ± 0.05	6.52 ± 0.05	1.40 ± 0.08	30 ± 4	8.04 ± 0.20	6.68 ± 0.07	1.36 ± 0.21	27 ± 10	0.04 ± 0.22	CL
2005 EO$_{304}$	6.57 ± 0.09	5.14 ± 0.11	1.43 ± 0.14	32 ± 6	8.09 ± 0.13	6.73 ± 0.14	1.36 ± 0.19	27 ± 8	0.07 ± 0.24	CL
Borasisi	6.69 ± 0.01	5.31 ± 0.01	1.43 ± 0.03	28 ± 1	7.15 ± 0.02	5.68 ± 0.01	1.47 ± 0.03	35 ± 1	−0.04 ± 0.04	CL
2001 QY$_{297}$	6.82 ± 0.22	5.34 ± 0.10	1.48 ± 0.24	36 ± 12	7.03 ± 0.28	5.78 ± 0.15	1.25 ± 0.31	21 ± 16	0.23 ± 0.39	CL

[a] Magnitude geometrically corrected (Appendix A, Eq. (A.4)) to account for heliocentric, geocentric distance, phase angle of observation and phase coefficient.
[b] Spectral gradient, a measure of the reddening of the reflectance spectrum between two wavelengths, V and I, expressed in percent of reddening per 100 nm.
[c] CL = Classical, CN = Centaur, SD = Scattered. Derived from the Deep Ecliptic Survey (DES) database, Elliot et al. (2005).
[d] Combined light values, the components were not uniquely resolved.

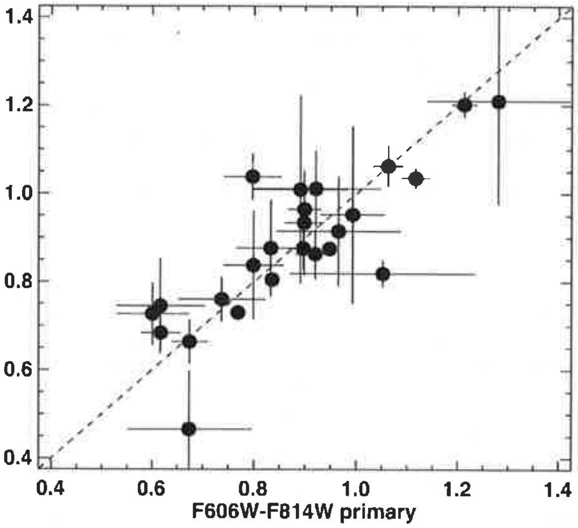

Fig. 1. The secondary vs. primary colors for each binary object are plotted. The dashed line demarks a slope of 1, indicating components of identical color. A Spearman rank test shows the primary and secondary colors correlated at the 99.99991% level (5-sigma for a normal distribution). A Pearson product-moment calculation yields a similar result.

5.2. Comparison to single TNOs

In Fig. 2 we plot a comparison of the colors of TNB components with the colors of assumed single TNOs from the MBOSS (Hainaut and Delsanti, 2002) and HST (Stephens and Noll, 2007) color databases. The TNB components appear to span the same color range as single TNOs. In order to evaluate the significance of the apparent similarity of binary colors with singles we carried out a K-S test. Using all of the data shown in Fig. 2 we find a high probability of correlation, 96% (Fig. 3). However there are possible biases in the data sample that could be important.

First, it is important to note that some fraction of the apparently single objects are likely to be binaries. For objects not yet observed by HST, it can be estimated that ~20% or more of Cold Classical objects and ~10% or fewer of the other dynamical classes (Noll et al., 2008a) are detectable binaries at HST WFPC2 resolution. However, a significant fraction of objects in MBOSS have already been searched for binaries with HST so the potential for resolvable binaries is limited. The distribution of binaries as a function of separation (Kern and Elliot, 2006; Noll et al., 2008a) suggests that a substantial fraction of binaries may exist, but be unresolvable by HST. Estimating the number of objects in the apparently single dataset is problematic. In the most extreme case, all TNOs could be binary. In that case, we would be comparing color as a function of binary separation.

A more tractable source of potential bias is related to the known correlation of color with dynamical class (Tegler and Romanishin, 2000; Gulbis et al., 2006). In particular, the Cold Classical population is known to be systematically redder than other dynamical classes. Because binaries are more common in the Cold Classical population, our sample of binaries is skewed with 44% Cold Classicals compared to 27% for the singles. To try to account for this bias we randomly selected 10 samples of singles with the same mixture of Cold Classicals and non-Cold Classicals as in our

Table 4
Groundbased and HST comparison.

Object	HST		MPC	Literature		
	H_V [a]	Spectral gradient	H_V	H_V [a]	Spectral gradient	Ref.
2001 QC_{298}	7.66 ± 0.03	1 ± 2	6.1	–	–	–
Teharon	5.97 ± 0.03	1 ± 2	5.5	–	–	–
2000 QL_{251}	7.02 ± 0.07	5 ± 5	6.3	–	–	–
(120347)	4.26 ± 0.02	2 ± 1	4.4	–	–	–
(60458)	7.43 ± 0.10	6 ± 7	6.8	6.97 ± 0.04	13 ± 2	2
				7.36 ± 0.02	1 ± 1	3
1998 WW_{31}	6.60 ± 0.01	6 ± 1	6.1	–	–	–
Typhon	7.75 ± 0.01	9 ± 1	7.2	7.68 ± 0.04	12 ± 2	1
				7.65 ± 0.02	0 ± 0	3
2001 XR_{254}	6.10 ± 0.04	10 ± 3	5.6	–	–	–
Ceto	6.43 ± 0.01	9 ± 1	6.3	6.60 ± 0.03	4 ± 3	3
Logos	6.72 ± 0.06	11 ± 6	6.6	6.76 ± 0.18	34 ± 7	2
(134860)	6.49 ± 0.06	20 ± 3	6.0	–	–	–
2004 PB_{108}	7.13 ± 0.12	15 ± 8	6.3	–	–	–
2003 TJ_{58}	7.39 ± 0.06	14 ± 3	7.8	–	–	–
(47171)	3.95 ± 0.01	17 ± 1	4.9	5.272 ± 0.055	47 ± 3	1
				4.86 ± 0.06	32 ± 2	2
				5.33 ± 0.02	16 ± 1	3
2001 FL_{185}	7.41 ± 0.21	18 ± 12	7.0	–	–	–
2000 CF_{105}	7.38 ± 0.14	18 ± 8	6.9	7.59	–	3
1999 OJ_4	7.49 ± 0.27	26 ± 14	7.0	6.91 ± 0.06	27 ± 4	2
(82075)	4.85 ± 0.10	21 ± 9	5.0	4.39 ± 0.06	19 ± 4	2
				4.74 ± 0.02	3 ± 3	3
(79360)	5.62 ± 0.02	24 ± 1	5.1	5.06 ± 0.09	28 ± 3	2
				5.52 ± 0.07	8 ± 4	3
2003 QW_{111}	7.14 ± 0.10	24 ± 5	6.4	–	–	–
(119979)	4.88 ± 0.07	23 ± 4	5.1	–	–	–
(123509)	6.77 ± 0.06	21 ± 4	6.5	–	–	–
(148780)	6.44 ± 0.07	26 ± 5	5.6	–	–	–
2003 QY_{90}	6.94 ± 0.03	26 ± 2	6.3	–	–	–
(80806)	7.10 ± 0.09	26 ± 5	6.3	6.30 ± 0.03	51 ± 30	2
(182933)	6.99 ± 0.06	27 ± 2	6.4	–	–	–
1999 RT_{214}	8.13 ± 0.02	30 ± 2	7.8	–	–	–
(26308)	5.98 ± 0.02	30 ± 1	5.8	5.80 ± 0.19	32 ± 5	2
				6.13 ± 0.10	23 ± 7	3
2000 CQ_{114}	7.21 ± 0.25	28 ± 13	6.8	–	–	–
2005 EO_{304}	6.33 ± 0.15	17 ± 10	6.3	–	–	–
Borasisi	6.25 ± 0.01	39 ± 1	5.9	–	22 ± 3	4
2001 QY_{297}	6.09 ± 0.03	25 ± 2	5.4	–	20 ± 3	4

(1) Rabinowitz et al. (2007); (2) Hainaut and Delsanti (2002); (3) Tegler et al. (2007); (4) Gulbis et al. (2006).

[a] Magnitude of the combined flux of the binary system (primary + secondary) geometrically corrected (Appendix A, Eq. (A.4)) to account for heliocentric, geocentric distance, phase angle of observation and phase coefficient.

binary data. We find that the correlation probability ranges from 60–96% in these ten tests. Any bias from the dynamical makeup of the sample appears to be small and if anything reduce the correlation. However, in general, the correlation remains high leading us to conclude that whatever mechanism is responsible for the colors of TNOs, it affects TNBs similarly.

5.3. *Color correlations*

How might the identical colors of the primary and the secondary in binaries have arisen? There are two possibilities. TNO colors could be the product of local environmental factors related to their current heliocentric orbit. In this case, because binary components share the same heliocentric orbits, the environmental effects related to their orbits are the same. Alternatively, identical colors may result if TNO colors are genetic. In this scenario, binary components have the same composition and color because each component accreted at the same location in the protoplanetary disk before becoming gravitationally bound. Finally, impacts can play a role both as an environmental factor and in the creation of bound systems from a single parent body. We discuss each of these different possibilities.

In addressing the origin of identical binary colors, it is worth keeping in mind the strong evidence that TNBs are primordial (cf. Noll et al., 2008a). System angular momentum indicates that dynamical capture is the only possible mode of formation for many TNBs. This formation mode requires a density much larger than currently exists in the Kuiper Belt (Goldreich et al., 2002). Similarly, collisional models that may account for the satellites of the largest TNOs, also require higher density of impactors than is found in the current Kuiper Belt (Canup, 2005; Levison and Morbidelli, 2007). Whether formed by capture or impact, binaries and multiples must have formed before the protoplanetary disk was depleted to its current anemic state.

5.3.1. *Current environment*

With the exception of the giant-planet crossing TNBs (42355) Typhon/Echidna and (65489) Ceto/Phorcys, the known binaries are currently found in orbits that are stable on Gyr timescales. Thus, if environmental factors play a role in determining the colors of TNOs, it should be possible to identify relationships between dynamical status and color in ensembles of objects.

A number of investigations have searched for measurable trends of color with current dynamical status. The strongest color trend that has been identified to date is the trend with inclination among Classical TNOs (cf. Doressoundiram et al., 2008; low inclination and eccentricity orbits). However, as shown by Thébault and Doressoundiram (2003), this trend cannot be explained by impact energy (Stern, 2002). Instead, this trend has generally been understood as a result of Classicals being composed of two over-

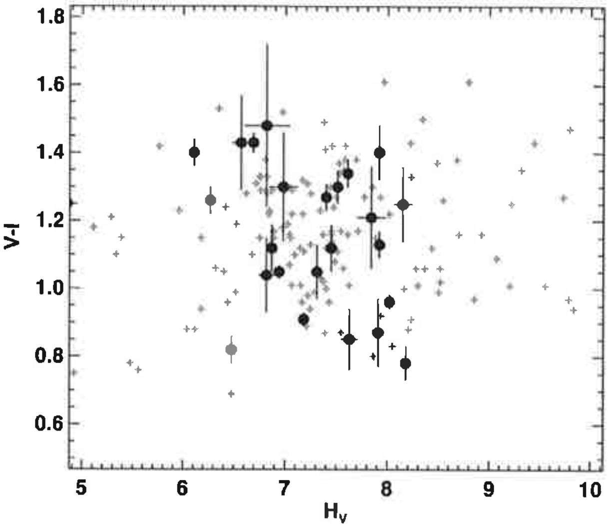

Fig. 2. V–I color vs. absolute magnitude is plotted. Only the colors of the primaries (circles) from this work are plotted for clarity. The binary colors occupy the same range as the colors of assumed single TNOs (gray crosses) taken from the MBOSS (Hainaut and Delsanti, 2002) and HST (Stephens and Noll, 2007) databases. Uncertainties on MBOSS colors are not shown for clarity, but are typically about ±0.05 magnitudes.

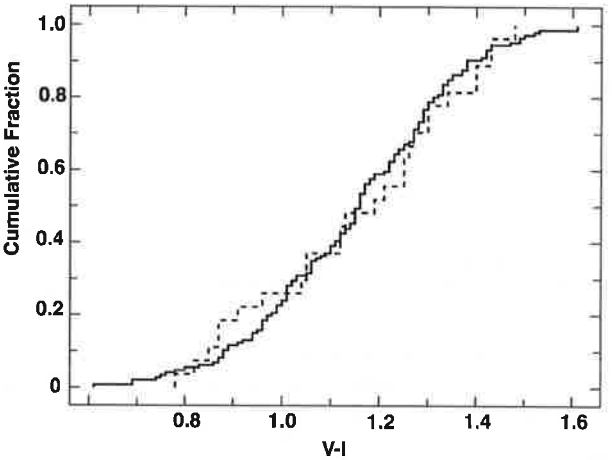

Fig. 3. K-S test for all MBOSS (Hainaut and Delsanti, 2002) and HST (Stephens and Noll, 2007) colors (V–I) compared to our HST binary color sample. Without selecting the objects with respect to their dynamical class we find a correlation probability of 96%. If we match the samples dynamically (same percentage of Cold Classical and non-cold-Classical objects in both the MBOSS + HST and TNB sample) we find that the correlation probability ranges from 60 to 96%. Clearly the TNB components span the same color range as single TNOs implying that whatever colors these objects affects binaries similarly.

lapping populations with intrinsically different colors. As argued by Noll et al. (2008a), the sharp difference in binaries between high and low inclination Classicals indicates that their physical differences, including color and albedo (Brucker et al., 2009; Grundy et al., 2005), are likely primordial.

The peak temperature of a TNO is a physical factor that might influence color. The peak temperature of a TNO is most closely related to its perihelion. However, equilibrium temperature varies only slowly, as $r^{-0.5}$, so that plausible temperature differences are on the order of 10 K or less. Albedo variations can produce a temperature effect nearly as large, as can pole orientation and thermal inertia. All of these unknowns conspire to confound the interpretation of any observed trends. In existing color surveys, no strong trend of TNO color with perihelion has been observed (Doressoundiram et al., 2008).

Variation in cosmic ray flux and solar wind is another mechanism that might affect the surface properties of TNOs. Solar wind flux drops off as $1/r^2$ as expected. However, beyond $\sim$10 AU the particle density is dominated by neutrals that remain roughly constant with heliocentric distance (Richardson and Schwadron, 2008). TNOs with aphelia greater than $\sim$100 AU may penetrate the asymmetric heliopause where they may be exposed to a flux of interstellar ions comparable in density to the neutrals. Cooper et al. (2003) calculate that the uppermost 10 nm accumulates 100 eV per atom in a relatively short $\sim 10^6$ yr timescale, although at depths of a micron or more the timescale is longer than the age of the Solar System. Taken together, there is little to suggest that particle irradiation can account for differences in TNO colors.

Micrometeorite gardening is another environmental factor that plays a role in space weathering. The plasma wave detectors on Voyager 1 and 2 found impact rates out to about 30 and 50 AU, respectively, to be roughly constant (Grün et al., 2000), ruling out variations in micrometeorite impacts as a source of global variation in TNO surfaces. The stochastic nature of impact resurfacing (Jewitt and Luu, 2001) makes it likely, however, that separate components in a binary would have different collisional histories and potentially strong color variation lightcurve signatures. The identity of binary component colors and lack of color variation (Section 5.4) is, therefore, evidence against impact resurfacing as a mechanism for creating the observed color diversity of TNOs.

For binaries we must also consider the unique microenvironment in which these objects reside. Stern (2008) has shown that for the largest TNOs, material ejected from the surfaces of small satellites remains gravitationally bound in the binary (or multiple) system and can lead to a shared surface regolith. However, as Stern also calculates, for the smaller TNOs in our sample, micrometeorite ejecta velocities exceed the escape velocity of the pair and the total mass accreted can be estimated simply as the total mass ejected by impacts times the fractional solid angle subtended by the object as seen from its companion.

Durda and Stern (2000) estimate the mass ejected by TNOs to be between $4\text{–}70 \times 10^{18}$ g $(r/100\ \text{km})^2$, where r is the radius of the target body. Following Stern (2008), the fraction of this mass that can be intercepted ranges from 10^{-6} to 5×10^{-4} for the systems with published binary orbits (Noll et al., 2008a; Table 2). This fraction results in mass per unit area ranging from 0.02 to 3.5 g cm^{-2}, or a layer 0.04 to 7 cm thick for density 0.5 g cm^{-3}. Stern points out that a layer this thick is enough to dominate the photometrically active surface. However, for this mechanism to work for the small, more equally sized binaries, one must postulate that the accumulating veneer of material from the companion body is undisturbed over the age of the Solar System at the same time that 2×10^3 to 10^6 times as much mass is being removed from the surface by impacts.

Observational tests of ejecta exchange are possible. Ejecta exchange in comparable mass binaries, like the ones that dominate our sample, would produce a color distribution with a smaller variance around the median of observed TNO colors than the general TNO population by "averaging" the component colors. However, as we describe in Section 5.2, the color distribution of TNBs is a very close match to that of TNOs in general. We conclude that the TNB color distribution shows no evidence of ejecta exchange among the objects measured in our sample. Another possible test occurs in tidally locked binaries which would produce facing hemispheres with a common color while oppositely facing hemispheres would retain their original colors. At present, however, there are few known synchronous binaries and little data to constrain colordependent lightcurves as we discuss in Section 5.4. Future observations may remedy this lack of data.

In summary, the comparability of TNB colors to the colors of apparently single TNOs argues that the influence of the current local environment, if any, on the colors of TNBs must be the same as it is for the general TNOs population. Thus, we conclude that there is little evidence that the environment in which TNBs have resided for the last 4 Gyr has had a determinative influence on their colors. The identity of binary component colors, is thus not explained by environmental factors.

5.3.2. *Composition*

If local environmental factors are not the source of color correlation in TNBs, then we must look to TNO genetics. Many TNOs, perhaps all, originated elsewhere in the protoplanetary disk than their current locations in the Kuiper Belt (Gomes et al., 2005; Morbidelli et al., 2005; Tsiganis et al., 2005; Levison et al., 2008). In some models, TNOs originated over a wide range of heliocentric distance from ~10 out to ~30 AU or more. Interestingly, this distance range spans several possible compositional thresholds, at increasing distances from the Sun, where hydrocarbons, methane, and carbon monoxide become stable solids (Ciesla and Cuzzi, 2006). TNO color diversity might then trace compositional differences in the protoplanetary disk, even allowing for subsequent space weathering.

Same-color binaries are a natural outcome if compositionally distinct zones or eddies (Nesvorny, 2008) were present in the protoplanetary disk. Because significantly higher densities are required for binary formation by both dynamical capture and collisions (Goldreich et al., 2002; Levison and Morbidelli, 2007), binaries must have formed before any substantial mixing of the disk occurred. Thus, the components in each binary can be expected to have identical compositions determined by the physical properties of the protoplanetary disk where they coalesced. Color then, emerges as an observable proxy for primordial composition as has been argued elsewhere (Tegler et al., 2008; Noll et al., 2008b). Interestingly, the fact that TNB colors span the same range as TNO colors also allows us to conclude that binary formation occurred at all locations in the protoplanetary disk and not in a preferred locale.

Collisions may also play a minor role in creating bound systems with identical surface composition and colors. 2003 EL_{61} and its associated family appear to be one such example (Brown et al., 2007; Levison and Morbidelli, 2007). However, most of the objects in our sample cannot have originated in this way and so, we conclude, collisions cannot be responsible for the global color properties of TNBs.

5.4. *Variability*

As part of our determination of the resolved colors of TNBs, we also assess the variability of the components. Two different approaches were followed.

First, we looked for evidence of short-period variability that might result from lightcurve variations. Because we calculated the uncertainties in our magnitudes based on the scatter of an object's measurements during the 90–180 min HST observation, the presence of real variation in the brightness of one or both components of a TNB will result in an inflated photometric uncertainty. At least one component of (148780) 2001 UQ_{18}, 2000 QL_{251}, 2001 QY_{297} and 2001 XR_{254} showed evidence of lightcurve variability during this timespan on the order of a few tenths of a magnitude. Further evaluation of the lightcurves of these objects will be addressed in a future paper after all the data for these objects have been obtained through our 11178 HST program. For now we note that the photometric uncertainty for these four objects may be partly inflated by lightcurve variations. The color measurements are consistent within the uncertainties across HST orbits indicating no substantial color variability.

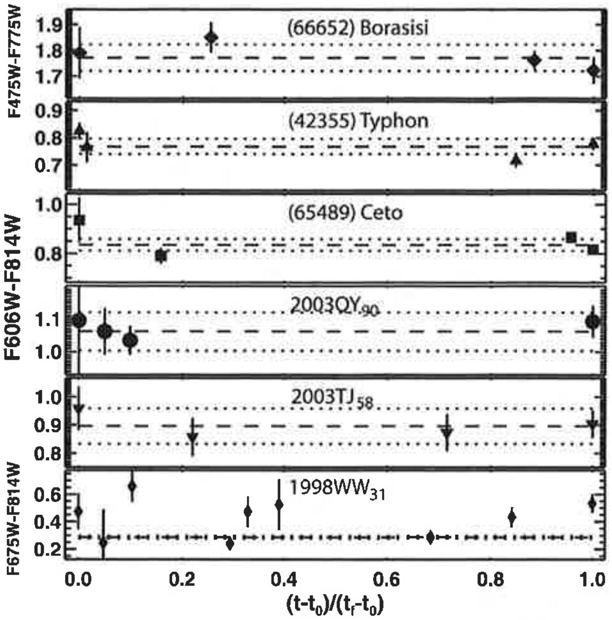

Fig. 4. Primary colors obtained at multiple epochs, t, are plotted as a function of days from the first observation t_0, normalized by the duration of observation for each object, t_f [(66652) Borasisi $t_f = 100.689$ days, (42355) Typhon $t_f = 306.380$ days, (65489) Ceto $t_f = 24.757$ days, 2003 QY_{90} $t_f = 419.776$ days, 2003 TJ_{58} $t_f = 78.249$ days, and 1998WW31 $t_f = 226.333$ days]. A dashed line is drawn at the weighted mean color for each object with a dotted line at the two sigma level above and below the average. (42355) Typhon, (65489) Ceto and 1998 WW_{31} each have at least one color measurement that deviates from the mean color by 2-sigma (the average individual error bar is 0.03–0.05 magnitudes).

Second, six TNBs had color measurements at multiple epochs (spanning as short as 24 days and as long as 419 days). We correct the magnitudes for different observational geometry (Appendix A, Eq. (A.4)) and plot in Fig. 4 the color variation of the primary component vs. time scaled to the duration of the observations [(42355) Typhon $t_f = 306.380$ days, (65489) Ceto $t_f = 24.757$ days, 2003 QY_{90} $t_f = 419.776$ days, 2003 TJ_{58} $t_f = 78.249$ days, 1998 WW_{31} $t_f = 226.333$ days and (66652) Borasisi $t_f = 100.689$ days]. In all cases the color of the secondary component is nearly identical to the primary so for clarity we only plot the primary component.

Overall, the colors of the TNOs are consistent between visits. In a few cases, the colors of the Centaurs and one of the TNOs, 1998 WW_{31}, there is variation off the median by slightly more (2-sigma) than the error bars (0.03 magnitudes) in one or more epochs, however with respect to the global statistics of the measurements, none of these variations are significant.

6. Conclusions

We have measured the colors of both components of 23 TNBs. TNBs display a wide range of colors, but within individual binary systems colors are strongly consistent. We find that the colors of the components are correlated at the 99.99991% level based on a Spearman rank calculation. They are also identical to each other within the measurement uncertainties. Colors of TNBs cover the same range as apparently single TNOs suggesting that there are no special mechanisms affecting the colors of binaries that are not operative on singles. The distributions are indistinguishable at the 96% level with a K-S test. Four objects show evidence for short duration (90–180 min) lightcurve variability, and three TNBs show hints of possible color variation, but the result is not strong.

We reviewed the possible environmental mechanisms that might produce correlated colors, but did not find any that could unambiguously produce correlated colors. The exchange of regolith caused by impacts (Stern, 2008) does allow for the accretion of small amounts of material on companions, but is likely dwarfed by the loss of material and other resurfacing effects caused by impacts. In the absence of a convincing environmental mechanism, we conclude that the correlated colors of binaries can be best explained if colors of TNBs, and TNOs in general, are the surface expression of compositional differences set in the protoplanetary nebula. Color gradients in circumstellar disks may reveal analogous processes in other planet-forming environments.

Acknowledgments

This work is based on observations made with the NASA/ESA Hubble Space Telescope. These observations are associated with programs 9991 and 11178. Support for these programs was provided by NASA through a grant from the Space Telescope Science Institute, which is operated by the Association of Universities for Research in Astronomy, Inc., under NASA Contract NAS 5-26555. We also wish to thank two anonymous reviewers and A. Stern for a prepublication copy of his 2008 paper.

Appendix A. HST photometry

It became clear during our analysis that there was no coherent comprehensive reference for photometric analysis of our HST datasets. We relied on a number of internal HST documents, the instrument handbooks as well some papers in the literature. Therefore, we provide in this appendix a complete description of our photometric pipeline to document our analysis and provide a cohesive reference point.

The calibrated magnitude, M_c, is a combination of 6 factors for both instruments, one that is obtained by direct measurement from the image, while the other five are offsets to correct for various aspects of the instrumentation. The summed components include:

$$M_c = M_{\rm half} + \Delta M_{\rm inf} + M_{\rm Zpt} + {\rm CTE} + M_{\rm vega} + \Delta M_{\rm STD}. \tag{A.1}$$

$M_{\rm half}$ is the measured component, summed counts, from a circular aperture that extends out to 0.5 arcsec placed around the source. Model PSFs created with Tiny Tim were shifted and scaled to match the flux of the primary and secondary in each binary system. The counts within a 0.5″ aperture were then summed for the individual primary and secondary models that reproduced the data. Two main effects come from using the models instead of the raw data: (1) the object counts are not noisy since they come from a model, and (2) our measured signal is not complicated by the signal from the binary companion. $M_{\rm inf}$ is read off of Table 5 in Sirianni et al. (2005) for the particular filter in which the observation is obtained for ACS/HRC and is 0.1 magnitudes for WFPC2 photometry irrespective of filter. It is a single factor that compensates for the additional flux of the object between 0.5″ and nominal "infinity," the standard reference point for *synphot*. $M_{\rm Zpt}$ is calculated from values provided in the image header keywords *photflam* and *photzpt* such that $\Delta M_{\rm Zpt} = -2.5\log(photflam) - photzpt$. However, this magnitude is still in the internal HST system, STmag, and needs to be converted to a standard stellar magnitude, referenced in *synphot* as the Vegamag system. We use a Kurucz solar model as our reference standard and find that the conversion factors, $M_{\rm Vega}$, for F606W and F814W are −0.2989 and −1.2376, respectively for WFPC2. Likewise, the factors are −0.2369 and −1.28 for ACS/HRC. Finally, there is a correction for where the object is located on the chip to account for deficits in charge transfer efficiency, CTE, an effect that causes some signal to be lost when charge is transferred down the chip during readout. The calculation for CTE is different for each instrument and the effect is more significant for WFPC2 than for ACS/HRC. To calculate CTE for WFPC2 we follow the example of Dolphin (2000a, 2000b) using the following equation set:

$$\begin{aligned}{\rm CTE} &= {\rm YCTE} + {\rm XCTE}\\ &= \frac{\ln(e^{c1} \times [1 + c2] - c2)}{0.436} + 0.0021 \times \frac{x}{800} e^{(-0.234 \times bg)},\end{aligned} \tag{A.2}$$

where

$$\begin{aligned}c1 &= 0.0114(0.67 \times e^{(-0.246 \times lbg)} + 0.330 \times e^{(-0.0359 \times bg)})\\ &\quad \times \left(1 + 0.335 \times yr - 0.0074 \times yr^2\right) \times \frac{y}{800},\\ c2 &= 3.55 e^{(-0.474 \times lct)},\\ lct0 &= \ln\left(\frac{\rm counts}{\rm electrons}\right) - 7,\\ bg &= \sqrt{\left[\frac{\rm background}{\rm electrons}\right]^2 + 1} - 10,\\ lbg &= \ln\left(\sqrt{\left[\frac{\rm background}{\rm electrons}\right]^2 + 1}\right) - 1,\\ yr &= \frac{(\rm MJD - 50193)}{365.25},\end{aligned}$$

and

$$lct = lct0 + 0.921 \times {\rm XCTE}.$$

For ACS/HRC we follow the process described by Riess (2003) and the equation set:

$$\begin{aligned}{\rm CTE} &= 10^{-0.89} \times {\rm SKY}^{-0.24} \times {\rm FLUX}^{-0.21} \times \frac{Y_{\rm pos}}{1024}\\ &\quad \times \frac{(\rm MJD - 52333)}{(52714 - 52333)}\end{aligned} \tag{A.3}$$

with the exponents for the first three parameters based on a 3 pixel aperture. The result of all of these components is the calibrated magnitude of the object in the observed HST filter in the standard Vegamag system.

For comparison with the standard Johnson–Cousins colors in the literature we perform one more conversion, from F606W to Johnson V and F814W to Cousins I. The values are different for each camera. The conversion actually requires two calculations since we want to find the offset using a solar spectrum of similar reddening as the object itself. Using *synphot* we create a number of look-up tables. We construct a table of F606W–F814W values vs. the reddening function (ebmv) for our Kurucz model (call this Table A) and a table of embv vs. filter conversions (F606-Johnson V, F814–Cousins I etc.; call this Table B). For a given object we take our measured F606W–F814W then use the table to look up the appropriate ebmv value for that object. We then find the offset values between the observed and desired filters with the Kurucz model reddened appropriately for the object. We add the offset value to the predetermined calibrated magnitude for our object in the HST filter system to find the actual magnitude of the object in standard filters. For example, F606W = 22.26 and F814W = 21.43 so F606W–F814W = 0.83. From Table A we find embv = 0.4. From Table B we find that $\Delta M_{\rm STD} = 0.345$ for F606W to Johnson V and $\Delta M_{\rm STD} = 0.007$ for F814W to Cousins I at this ebmv value. Our final magnitudes are: V = 22.60 and I = 21.43 so V–I = 1.17. To determine the uncertainties we consider the minimum and maximum deltas in the natural HST filters (found from Table A) to identify the range of magnitude offsets in Table B and propagate the uncertainties from there. The uncertainty in V grows more than the uncertainty in I since the shift in wavelength is larger from F606W to Johnson V than F814W to Cousins I.

Finally, so that our measurements can easily be compared with observations under different geometric circumstances, we calculate the H-magnitude (the mean magnitude of a small body in the absence of rotational or aspect variations at a solar phase angle α, reduced to heliocentric and geocentric distances of 1 AU) in the respective filters and record them in Table 2. We follow the methodology of Bowell et al. (1989) as applied to the Kuiper Belt following the pattern of Romanishin and Tegler (2005). In Eq. (A.4) r is heliocentric distance (AU), Δ is geocentric distance (AU), and α is the Sun-target-observer angle (degrees) at the time of observation. We do not have information for constraining G so we use the value adopted in the literature of 0.15 (Romanishin and Tegler, 2005),

$$\begin{aligned} H_{\text{filter}} &= M_{\text{filter}} - 5\log(r\Delta) \\ &\quad + 2.5\log\big[(1-G)\Phi_1(\alpha) + G\Phi_2(\alpha)\big], \end{aligned} \tag{A.4}$$

where

$$\phi_1(\alpha) = \exp\left[-3.33\left(\tan\frac{1}{2}\alpha\right)^{0.63}\right] \quad \text{and}$$

$$\phi_2(\alpha) = \exp\left[-1.87\left(\tan\frac{1}{2}\alpha\right)^{1.22}\right].$$

References

Baggett, S., and 22 colleagues, 2002. In: Mobasher, B. (Ed.), HST WFPC2 Data Handbook: Version 4.0. STScI, Baltimore.

Barucci, M.A., ESO Large Program Team, 2008. TNO ESO-VLT Large Program (2006–2008): Results and implications. In: Asteroids, Comets, Meteors. Abstract 8128.

Bauer, J.M., Meech, K.J., Fernandez, Y.R., Pittichova, J., Hainaut, O.R., Boehnhardt, H., Delsanti, A.C., 2003. Physical survey of 24 Centaurs with visible photometry. Icarus 166, 195–211.

Boehnhardt, H., Tozzi, G.P., Birkle, K., Hainaut, O., Sekiguchi, T., Vair, M., Watanabe, J., Rupprecht, G., The FORS Instrument Team, 2001. Visible and near-IR observations of transneptunian objects: Results from ESO and Calar Alto Telescopes. Astron. Astrophys. 378, 653–667.

Boehnhardt, H., Delsanti, A., Barucci, A., Hainaut, O., Doressoundiram, A., Lazzarin, M., Barrera, L., de Bergh, C., Birkle, K., Dotto, E., Meech, K., Ortiz, J.E., Romon, J., Sekiguchi, T., Thomas, N., Tozzi, G.P., Watanabe, J., West, R.M., 2002. ESO Large Program on physical studies of transneptunian objects and Centaurs: Visible photometry—First results. Astron. Astrophys. 395, 297–303.

Bowell, E., Hapke, B., Domingue, D., Lumme, K., Peltoniemi, J., Harris, A.W., 1989. Application of photometric models to asteroids. In: Binzel, R.P., Gehrels, T., Matthews, M.S. (Eds.), Asteroids II. Univ. of Arizona Press, Tucson, pp. 524–556.

Brown, M.E., Barkume, K.M., Ragozzine, D., Schaller, E.L., 2007. A collisional family of icy objects in the Kuiper belt. Nature 446, 294–296.

Brucker, M.J., Grundy, W.M., Stansberry, J.A., Spencer, J.R., Sheppard, S.S., Chiang, E.I., Buie, M.W., 2009. High albedos of low inclination classical Kuiper belt objects. Icarus, in press.

Brunetto, R., Roush, T.L., 2008. Impact of irradiated methane ice crusts on compositional interpretations of TNOs. Astron. Astrophys. 481, 879–882.

Canup, R.M., 2005. A giant impact origin of Pluto–Charon. Science 307, 546–550.

Ciesla, F.J., Cuzzi, J.N., 2006. The evolution of the water distribution in a viscous protoplanetary disk. Icarus 181, 178–204.

Cooper, J.F., Christian, E.R., Richardson, J.D., Wang, C., 2003. Proton irradiation of centaur, Kuiper belt, and Oort cloud objects at plasma to cosmic ray energy. Earth Moon Planets 92, 261–277.

Delsanti, A.C., Boehnhardt, H., Barrera, L., Meech, K.J., Sekiguchi, T., Hainaut, O.R., 2001. BVRI photometry of 27 Kuiper belt objects with ESO/very large telescope. Astron. Astrophys. 380, 347–358.

Delsanti, A., Hainaut, O., Jourdeuil, E., Meech, K.J., Boehnhardt, H., Barrera, L., 2004. Simultaneous visible-near IR photometric study of Kuiper belt object surfaces with the ESO/very large telescopes. Astron. Astrophys. 417, 1145–1158.

Dolphin, A.E., 2000a. The charge-transfer efficiency and calibration of WFPC2. Publ. Astron. Soc. Pacific 112, 1397–1410.

Dolphin, A.E., 2000b. WFPC2 stellar photometry with HSTPHOT. Publ. Astron. Soc. Pacific 112, 1383–1396.

Doressoundiram, A., Peixinho, N., de Bergh, C., Fornasier, S., Thebault, P., Barucci, M.A., Veillet, C., 2002. The color distribution in the Edgeworth–Kuiper belt. Astron. J. 124, 2279–2296.

Doressoundiram, A., Peixinho, N., Doucet, C., Mousis, O., Barucci, A.M., Petit, J.M., Veillet, C., 2005. The Meudon multicolor survey (2MS) of centaurs and trans-neptunian objects: Extended dataset and status on the correlations reported. Icarus 174, 90–104.

Doressoundiram, A., Boehnhardt, H., Tegler, S.C., Trujillo, C., 2008. Color properties and trends of the transneptunian objects. In: Barucci, M.A., Boehnhardt, H., Cruikshank, D.P., Morbidelli, A. (Eds.), The Solar System Beyond Neptune. Univ. of Arizona Press, Tucson, pp. 91–104.

Durda, D.D., Stern, S.A., 2000. Collision rates in the present-day Kuiper belt and Centaur regions: Applications to surface activation and modification on comets, Kuiper belt objects, Centaurs, and Pluto–Charon. Icarus 145, 220–229.

Elliot, J.L., Kern, S.D., Clancy, K.B., Gulbis, A.A.S., Millis, R.L., Buie, M.W., Wasserman, L.H., Chiang, E.I., Jordan, A.B., Trilling, D.E., Meech, K.J., 2005. The deep ecliptic survey: A search for Kuiper belt objects and Centaurs. II. Dynamical classification, the Kuiper belt plane, and the core population. Astron. J. 129, 1117–1162.

Gil-Hutton, R., Licandro, J., 2001. VR photometry of sixteen Kuiper belt objects. Icarus 152, 246–250.

Goldreich, P., Lithwick, Y., Sari, R., 2002. Formation of Kuiper-belt binaries by dynamical friction and three-body encounters. Nature 420, 643–646.

Gomes, R., Levison, H.F., Tsiganis, K., Morbidelli, A., 2005. Origin of the cataclysmic late heavy bombardment period of the terrestrial planets. Nature 435, 466–469.

Grün, E., Krüger, H., Landgraf, M., 2000. Dust measurements in the outer Solar System. In: Fitzsimmons, A., Jewitt, D., West, R.M. (Eds.), Minor Bodies in the Outer Solar System: Proceedings of the ESO Workshop. Springer-Verlag, Germany, p. 99.

Grundy, W.M., 2009. Is the missing ultra-red material colorless ice? Icarus, in press.

Grundy, W.M., Noll, K.S., Stephens, D.C., 2005. Diverse albedos of small trans-neptunian objects. Icarus 176, 184–191.

Grundy, W.M., Stansberry, J.A., Noll, K.S., Stephens, D.C., Trilling, D.E., Kern, S.D., Spencer, J.R., Cruikshank, D.P., Levison, H.F., 2007. The orbit, mass, size, albedo and density of (65489) Ceto/Phorcys: A tidally-evolved binary Centaur. Icarus 191, 286–297.

Grundy, W.M., Noll, K.S., Virtanen, J., Muinonen, K., Kern, S.D., Stephens, D.C., Stansberry, J.A., Levison, H.F., Spencer, J.R., 2008. (42355) Typhon–Echidna: Scheduling observations for binary orbit determination. Icarus 197, 260–268.

Grundy, W.M., Noll, K.S., Buie, M.W., Benecchi, S.D., Stephens, D.C., Stansberry, J.A., Levison, H.F., 2009. Mutual orbits and masses of six transneptunian binaries. Icarus, in press.

Gulbis, A.S., Elliot, J.L., Kane, J.F., 2006. The color of the Kuiper belt core. Icarus 183, 168–178.

Hainaut, O.R., Delsanti, A.C., 2002. Colors of minor bodies in the outer Solar System: A statistical analysis. Astron. Astrophys. 389, 641–664.

Heyer, I., and 34 colleagues, 2004. WFPC2 Instrument Handbook: Version 9.0. STScI, Baltimore.

Jacobson, S., Margot, J.L., 2007. Colors of TNO binaries and evidence for a triple system from HST observations. Bull. Am. Astron. Soc. 39, 5211.

Jewitt, D., Luu, J., 1998. Optical-infrared spectral diversity in the Kuiper belt. Astron. J. 115, 1667–1670.

Jewitt, D.C., Luu, J.X., 2001. Colors and spectra of Kuiper belt objects. Astron. J. 122, 2099–2114.

Kern, S.D., 2006. A study of binary Kuiper belt objects. Ph.D. thesis, Massachusetts Institute of Technology: Earth, Atmospheric and Planetary Sciences.

Kern, S.D., Elliot, J.L., 2006. The frequency of binary Kuiper belt objects. Astrophys. J. 643, 57–60.

Krist, J., Hook, R., 2004. The Tiny Tim User's Guide: Version 6.3. STScI, Baltimore.

Lacerda, P., Luu, J., 2006. Analysis of the rotational properties of Kuiper belt objects. Astron. J. 131, 2314–2326.

Levison, H.F., Morbidelli, A., 2007. Models of the collisional damping scenario for ice-giant planets and Kuiper belt formation. Icarus 189, 196–212.

Levison, H.F., Morbidelli, A., Vanlaerhoven, C., Gomes, R., Tsiganis, K., 2008. Origin of the structure of the Kuiper belt during a dynamical instability in the orbits of Uranus and Neptune. Icarus 196, 258–273.

Luu, J., Jewitt, D., 1996. Color diversity among the Centaurs and Kuiper belt objects. Astron. J. 112, 2310–2318.

Margot, J.L., Brown, M.E., Trujillo, C.A., Sari, R., Stansberry, J.A., 2005. Kuiper belt binaries: Masses, colors and a density. Bull. Am. Astron. Soc. 37, 737.

McBride, N., Green, S.F., Davies, J.K., Tholen, D.J., Sheppard, S.S., Whiteley, R.J., Hillier, J.K., 2003. Visible and infrared photometry of Kuiper belt objects: Searching for evidence of trends. Icarus 161, 501–510.

Morbidelli, A., Levison, H.F., Tsiganis, K., Gomes, R., 2005. Chaotic capture of Jupiter's Trojan asteroids in the early Solar System. Nature 435, 462–465.

Nesvorny, D., 2008. Formation of Kuiper Belt binaries. Bull. Am. Astron. Soc. 40. Abstract 38.02.

Noll, K.S., Stephens, D.C., Grundy, W.M., Millis, R.L., Spencer, J., Buie, M.W., Tegler, S.C., Romanishin, W., Cruikshank, D.P., 2002. Detection of two binary trans-neptunian objects, 1997 CQ29 and 2000 CF105, with the Hubble Space telescope. Astron. J. 124, 3424–3429.

Noll, K.S., Stephens, D.C., Grundy, W.M., Osip, D.J., Griffin, I., 2004a. The orbit and albedo of trans-neptunian binary (58534) 1997 CQ29. Astron. J. 128, 2547–2552.

Noll, K.S., Stephens, D.C., Grundy, W.M., Griffin, I., 2004b. The orbit, mass, and albedo of transneptunian binary (66652) 1999 RZ253. Icarus 172, 402–407.

Noll, K.S., Grundy, W.M., Chiang, E.I., Margot, J.L., Kern, S.D., 2008a. Binaries in the Kuiper belt. In: Barucci, M.A., Boehnhardt, H., Cruikshank, D.P., Morbidelli, A. (Eds.), The Solar System Beyond Neptune. Univ. of Arizona Press, Tucson, pp. 345–364.

Noll, K.S., Grundy, W.M., Stephens, D.C., Levison, H.F., Kern, S.D., 2008b. Evidence for two populations of classical transneptunian objects: The strong inclination dependence of classical binaries. Icarus 194, 758–768.

Ortiz, J.L., Gutierrez, P.J., Casanova, V., Sota, A., 2003. A study of short term rotational variability in TNOs and Centaurs from Sierra Nevada observatory. Astron. Astrophys. 407, 1149.

Osip, D.J., Kern, S.D., Elliot, J.L., 2003. Physical characterization of the binary Edgeworth–Kuiper belt object 2001 QT297. Earth Moon Planets 92, 409–421.

Osip, D.J., Phillips, M.M., Bernstein, R., Burley, G., Dressler, A., Elliot, J.L., Persson, E., Shectman, S.A., Thompson, I., 2004. First-generation instruments for the Magellan telescopes: Characteristics, operation, and performance. In: Moorwood, A.F.M., Masanori, I. (Eds.), Ground-Based Instrumentation for Astronomy. In: Proc. SPIE, vol. 5492, pp. 49–59.

Pavlovsky, C., 2006. ACS Data Handbook, Version 5.0. Space Telescope Science Institute, Baltimore.

Peixinho, N., Doressoundiram, A., Romon-Martin, J., 2002. Visible-IR colors and lightcurve analysis of two bright TNOs: 1999TC36 and1998SN165. New Astron. 7, 359.

Peixinho, N., Boehnhardt, H., Belskaya, I., Doressoundriam, A., Barucci, M.A., Delsanti, A., 2004. ESO Large Program on Centaurs and TNOs: Visible colors—Final results. Icarus 170, 153–166.

Press, W.H., Teukolsky, S.A., Vetterling, W.T., Flannery, B.P., 1992. Numerical Recipes in C, second ed. Cambridge University Press, New York.

Rabinowitz, D.L., Schaefer, B.E., Tourtellotte, S.W., 2007. The diverse solar phase curves of distant icy bodies. I. Photometric observations of 18 trans-neptunian objects, 7 Centaurs, and Nereid. Astron. J. 133, 26–43.

Richardson, J.D., Schwadron, N.A., 2008. The limits of our Solar System. In: Barucci, M.A., Boehnhardt, H., Cruikshank, D.P., Morbidelli, A. (Eds.), The Solar System Beyond Neptune. Univ. of Arizona Press, Tucson, pp. 443–463.

Riess, A., 2003. On-orbit calibration of ACS CTE corrections for photometry. Instrument Science Report ACS, 2003-009.

Romanishin, W., Tegler, S.C., 2005. Accurate absolute magnitudes for Kuiper belt objects and Centaurs. Icarus 179, 523–526.

Sirianni, M., Jee, M.J., Benítez, N., Blakeslee, J.P., Martel, A.R., Meurer, G., Clampin, M., De Marchi, G., Ford, H.C., Gilliland, R., Hartig, G.F., Illingworth, G.D., Mack, J., McCann, W.J., 2005. The photometric performance and calibration of the Hubble space telescope advanced camera for surveys. Publ. Astron. Soc. Pacific 117, 1049–1112.

Sheppard, S.S., Jewitt, D.C., 2002. Time-resolved photometry of Kuiper belt objects: Rotations, shapes and phase functions. Astron. J. 124, 1757–1775.

Sheppard, S.S., Jewitt, D.C., 2003. Hawaii Kuiper belt variability project: An update. Earth Moon Planets 92, 207.

Spencer, J.R., Stansberry, J.A., Grundy, W.M., Noll, K.S., 2006. A low density for binary Kuiper belt object (26308) 1998 SM165. Bull. Am. Astron. Soc. 38, 3401.

Stansberry, J.A., Grundy, W.M., Margot, J.L., Cruikshank, D.P., Emery, J.P., Rieke, G.H., Trilling, D.E., 2006. The albedo, size and density of binary Kuiper belt object (47171) 1999 TC36. Astrophys. J. 643, 556–566.

Stephens, D.C., Noll, K.S., 2007. Visible and near-infrared photometry of transneptunian objects observed with HST. Bull. Am. Astron. Soc. 39, 491. Abstract.

Stephens, D.C., Noll, K.S., Grundy, W.M., Millis, R.L., Spencer, J.R., Buie, M.W., Tegler, S.C., Romanishin, W., Cruikshank, D.P., 2003. HST photometry of trans-neptunian objects. Earth Moon Planets 92, 251–260.

Stern, S.A., 2002. Implications regarding the energetics of the collisional formation of Kuiper belt satellites. Astron. J. 124, 2300–2304.

Stern, S.A., 2008. Ejecta exchange, color evolution in the Pluto system, and implications for KBOs and asteroids with satellites. Icarus, in press.

Tegler, S.C., Romanishin, W., 2000. Extremely red Kuiper-belt objects in near-circular objects beyond 40 AU. Nature 407, 979–981.

Tegler, S.C., Romanishin, W., Consolmagno, G., 2007. http://www.physics.nau.edu/~tegler/research/survey.htm.

Tegler, S.C., Bauer, J.M., Romanishin, W., Peixinho, N., 2008. Colors of Centaurs. In: Barucci, M.A., Boehnhardt, H., Cruikshank, D.P., Morbidelli, A. (Eds.), The Solar System Beyond Neptune. Univ. of Arizona Press, Tucson, pp. 105–114.

Thébault, P., Doressoundiram, A., 2003. Colors and collision rates within the Kuiper belt: Problems with the collisional resurfacing scenario. Icarus 162, 27–37.

Trujillo, C.A., Brown, M.W., 2002. A correlation between inclination and color in the classical Kuiper belt. Astrophys. J. 566, 125–128.

Tsiganis, K., Gomes, R., Morbidelli, A., Levison, H.F., 2005. Origin of the orbital architecture of the giant planets of the Solar System. Nature 435, 459–461.

Veillet, C., Parker, J.W., Griffin, I., Marsden, B., Doressoundiram, A., Buie, M., Tholen, D.J., Connelley, M., Holman, M.J., 2002. The binary Kuiper-belt object 1998 WW31. Nature 416, 711–713.